Global simulation of the Geospace Environment Modeling substorm challenge event

J. Raeder,[1] R. L. McPherron,[1] L. A. Frank,[2] S. Kokubun,[3] G. Lu,[4] T. Mukai,[5]
W. R. Paterson,[2] J. B. Sigwarth,[2] H. J. Singer,[6] and J. A. Slavin[7]

Abstract. We use a global model of Earth's magnetosphere and ionosphere to simulate the Geospace Environment Modeling (GEM) substorm challenge event of November 24, 1996. We compare our results to International Monitor for Auroral Geomagnetic Effects (IMAGE) ground magnetometer data, assimilative mapping of ionospheric electrodynamics (AMIE) polar cap potential and field aligned current patterns, Polar Visible Imaging System (VIS) estimates of the polar cap magnetic flux, GOES 8 geosynchronous magnetometer data, IMP 8 magnetometer data, and Geotail plasma and magnetic field data. We find generally good agreement between the simulation and the data. The modeled evolution of this substorm generally follows the phenomenological near-Earth neutral line model. However, reconnection in the tail is very localized, which makes establishing a causal relation between tail dynamics and auroral dynamics difficult, if not impossible. We also find that the model results critically depend on the parameterization of auroral Hall and Pedersen conductances and anomalous resistivity in the magnetosphere. For many combinations of parameters that enter these parameterizations, no substorm develops in the model, but instead the magnetosphere enters a steady convection mode. The main deviation of the model from the data is excessive convection, which leads to a strong, driven westward electrojet in the growth phase, only partial tail loading, and a reduced recovery phase. Possible remedies are a better model for auroral conductances, an improved anomalous resistivity model, and a more realistic treatment of the ring current.

1. Introduction

One of the goals of the Geospace Environment Modeling (GEM) substorm campaigns is the evaluation of current models of Earth's space environment and an assessment of how well they can predict the eminent features of substorms. What makes this task particularly difficult is the fact that no universally accepted model of the substorm morphology exists, let alone a model that would explain the physics of a substorm. Nevertheless, in order to make progress, a rigorous comparison of models with data needs to be made, because only in this way can the particular strengths and short-comings of models become apparent. On the basis of such assessments, improvements to the models, and thus to our understanding of the substorm process, can then be made.

The most comprehensive ab initio models of Earth's space environment are based on numerically solving the magnetohydrodynamic (MHD) equations. Several such models exist [*Lyon et al.*, 1998; *Ogino*, 1986; *Winglee and Menietti*, 1998; *Gombosi et al.*, 1998; *Tanaka*, 1995; *Janhunen et al.*, 1995; *Raeder*, 1999] and have been used to various extents to model substorms. Several of these models also include an ionosphere model and solve the electrodynamic coupling between the ionosphere and the magnetosphere self-consistently. It has been argued that the ionosphere controls to a large extent magnetospheric convection [*Fedder and Lyon*, 1987; *Raeder et al.*, 1996], although not in a sub-storm context. In this paper we will provide further evidence that this is the case; in particular, we will show that ionospheric conductance, as well as anomalous resistivity, can determine whether the magnetosphere enters a steady magnetospheric convection (SMC) mode or a convection mode during which a substorm develops.

MHD models generally predict a substorm evolution [*Lyon et al.*, 1998; *Goodrich et al.*, 1998; *Pulkkinen et al.*, 1998;

---

[1]Institute of Geophysics and Planetary Physics, University of California, Los Angeles.
[2]Department of Physics and Astronomy, University of Iowa, Iowa City.
[3]Solar-Terrestrial Environment Laboratory, Nagoya University, Toyokawa, Japan.
[4]High Altitude Observatory, National Center for Atmospheric Research, Boulder, Colorado.
[5]Institute of Space and Astronautical Science, Sagamihara, Japan.
[6]Space Environment Center, National Oceanic and Atmospheric Administration, Boulder, Colorado.
[7]Goddard Space Flight Center, National Aeronautics and Space Administration, Greenbelt, Maryland.

Walker et al., 1993; *Raeder*, 1995; *Raeder and McPherron*, 1998] that closely resembles the predictions of the near-Earth neutral line (NENL) model [*McPherron et al.*, 1973b; *McPherron*, 1991; *Baker et al.*, 1996, 1999]. In particular, the substorm expansion phase onset is closely associated with the formation of a new near-Earth neutral line. However, it is generally difficult to define with precision what constitutes the onset in the model. Experimentally, the onset is usually defined by either the brightening of the aurora, negative bays at auroral latitudes, or Pi2 pulsations. These signatures can usually be timed to within ∼2 min [see *Lyons et al.*, this issue(a), this issue(b)]. Simulations do not (yet) provide Pi2 pulsations. Although auroral emissions have been modeled using global simulations [*Fedder et al.*, 1995], the auroral features are still too poorly defined in space and time to use them for defining the onset precisely. Negative bays, on the other hand, can be modeled and are used in this study. Modeling the ground magnetic perturbations is particularly useful because it allows us to compare the temporal and spatial evolution of the electrojet in detail.

In the remainder of this paper we will first describe our model, in particular, the computation of ionospheric conductances and ground magnetic perturbations. We then compare results from our model with ground magnetometers, assimilated mapping of ionospheric electrodynamics (AMIE) potential and field aligned current (FAC) estimates, estimates of the polar cap magnetic flux from the Polar Visible Imaging System (VIS) imager, GOES 8 magnetometer data, IMP 8 magnetic field data, and Geotail plasma and field data. We then summarize and discuss our findings.

2. The Model

For this study we use a global numerical model of Earth's space environment that is principally based on a MHD description of the plasma. An integral part of this simulation code is an ionospheric model for the closure of field-aligned currents. In order to accommodate the large simulation volume with a long tail and long simulation times, the simulation code is parallelized for running on Multiple Instruction-Multiple Data (MIMD) machines by using a domain decomposition technique [*Fox et al.*, 1988] and message passing. The model solves the ideal MHD equations (modified as described in section 2.1) for the magnetosphere and a potential equation for the ionosphere. Numerical effects, such as diffusion, viscosity, and resistivity, are necessarily introduced by the numerical methods. These permit viscous interactions and to a limited extent magnetic field reconnection. The only explicit diffusive term is the anomalous resistivity that is included in Ohm's law. The effects of numerical diffusion and the anomalous resistivity term are discussed by *Raeder et al.* [1996] and *Raeder* [1999]. In this paper we will provide a further assessment of anomalous resistivity on substorm development.

2.1. Outer Magnetosphere

The magnetospheric (MHD) part of the model is solved using a finite difference method which is conservative for the gas dynamic part of the normalized MHD equations:

$$\frac{\partial \rho}{\partial t} = -\nabla \cdot (\rho \mathbf{v}), \tag{1}$$

$$\frac{\partial \rho \mathbf{v}}{\partial t} = -\nabla \cdot (\rho \mathbf{v}\mathbf{v} + p\mathsf{I}) + \mathbf{j} \times \mathbf{B}, \tag{2}$$

$$\frac{\partial e}{\partial t} = -\nabla \cdot (\{e + p\}\mathbf{v}) + \mathbf{j} \cdot \mathbf{E}, \tag{3}$$

$$\frac{\partial \mathbf{B}}{\partial t} = -\nabla \times \mathbf{E}, \tag{4}$$

$$\nabla \cdot \mathbf{B} = 0, \tag{5}$$

$$\mathbf{E} = -\mathbf{v} \times \mathbf{B} + \eta \mathbf{j}, \tag{6}$$

$$\mathbf{j} = \nabla \times \mathbf{B}, \tag{7}$$

$$e = \frac{1}{2}\rho v^2 + \frac{p}{\gamma - 1}, \tag{8}$$

where the symbols have their usual meanings, that is, $\mathbf{B}$ is the magnetic field, $\mathbf{E}$ is the electric field, ρ is the mass density, $\mathbf{v}$ is the plasma velocity, e is the plasma energy density, p is the plasma pressure, $\mathbf{j}$ is the current density, and γ is the ratio of specific heats, taken to be 5/3 in the simulations presented here. The $\mathbf{j} \times \mathbf{B}$ and $\mathbf{E} \cdot \mathbf{j}$ terms are treated as source terms because the very low plasma β and the large magnetic field gradients near the Earth do not allow the use of the full conservative form of the MHD equations. The model of the anomalous resistivity is given by

$$\eta = \alpha \mathrm{H}(j' - \delta)(j')^2, \tag{9}$$

$$j' = \frac{|j|\Delta}{|B| + \epsilon}, \tag{10}$$

where H is the Heaviside function, j is the local current density, B is the local magnetic field, Δ is the grid spacing, and ϵ is a very small number introduced to avoid dividing by zero. The normalized current density j' ($0 \leq j' \leq 1$) is used as a switch for the resistivity. In places where the resistivity is switched on it becomes proportional to the square of the local current density. Similar resistivity models have been used in the past to model the kinetic effects that lead to anomalous resistivity [*Sato and Hayashi*, 1979; *Hoshino*, 1991; *Otto*, 2000]. The parameters α and δ determine the value of the resistivity and the current density threshold that must be reached for the resistivity to be switched on. These parameters are chosen such that the resistivity η is nonzero only at a very few grid points in strong current sheets. Numerical values for δ and α will be given in section 4.5. The anomalous resistivity is assumed to be caused by kinetic instabilities and the resulting plasma turbulence. Although no generally accepted theory exists describing these phenomena, experimental evidence and justification for including an anomalous resistivity term is given by the observations of strong electromagnetic wave activity in the tail [*Sigsbee et al.*, this issue; see also *Cattell and Mozer*, 1986; *Cattell*, 1996; *Cattell et al.*, 1998].

The numerical grid is rectangular and nonuniform with the highest spatial resolution (∼0.3 R_E) near Earth and in the tail plasma sheet. It extends 19 R_E in the sunward direction, 300 R_E in the tailward direction, and ±40 R_E in the

Y and *Z* directions. The gasdynamic part of the equations is spatially differenced by using a technique in which fourth-order fluxes are hybridized with first-order (Rusanov) fluxes [*Harten and Zwas*, 1972; *Hirsch*, 1990]. The magnetic induction equation is treated somewhat differently [*Evans and Hawley*, 1988] in order to conserve $\nabla \cdot \mathbf{B} = 0$ exactly. The time-stepping scheme for all variables consists of a low-order predictor with a time-centered corrector, which is accurate to the second order in time. Thus the numerical scheme is flux-limited, that is, it produces diffusion only to the extent needed at shocks and discontinuities. In regions where all variables vary smoothly, the gas-dynamic variables are computed with fourth-order accuracy, and the magnetic field is computed with second-order accuracy. The outer boundary conditions are fixed at the given solar wind values on the upstream side. At the other boundaries we apply open, i.e., zero normal derivative, boundary conditions.

2.2. Ionosphere

The inner boundary, where the MHD quantities are connected to the ionosphere, is taken to be a shell of radius 3.5 R_E centered at Earth. The choice of this radius is a compromise necessitated by numerical considerations, such as extraneously high Alfvén speeds (up to a fraction of the speed of light) and very large magnetic field gradients closer to the Earth. However, this choice allows for the proper mapping of all relevant field-aligned current (FAC) systems down to $\sim 59^o$ magnetic latitude. The placement of the inner boundary also inhibits the formation of a ring current. Inside this shell we do not solve the MHD equations but assume a static dipole field. The important physical processes earthward of that shell are the flow of FACs and the closure of these currents in the ionosphere. Every few time steps (corresponding to a time interval of less than 5 s in real time) we use the static dipole field to map the magnetospheric FACs from the 3.5 R_E shell onto the polar cap. We then use the FACs as input for the ionospheric potential equation:

$$\nabla \cdot \Sigma \cdot \nabla \Phi = -j_\parallel \sin I, \tag{11}$$

which is solved on the surface of a sphere with a radius of 1.015 R_E, i.e., at 110-km altitude. Here Φ denotes the ionospheric potential as a function of magnetic latitude and local time, Σ is the tensor of the ionospheric conductance, $j_\parallel$ is the mapped FAC with the downward current considered positive and scaled for flux tube convergence, and I is the inclination of the dipole field at the ionosphere. The boundary condition $\Phi = 0$ is applied at the equator. For the ionospheric Hall and Pedersen conductances, Σ_H and Σ_P, which enter the conductance tensor Σ [*Kamide and Matsushita*, 1979], three ionization sources are taken into account. First, for the solar EUV ionization we use an empirical model [*Moen and Brekke*, 1993] that depends only on the solar 10.7-cm flux ($F_{10.7}$) and the solar zenith angle (χ):

$$\Sigma_H = (F_{10.7})^{0.53}(0.81k + 0.54k^{1/2}), \tag{12}$$

$$\Sigma_P = (F_{10.7})^{0.49}(0.34k + 0.93k^{1/2}), \tag{13}$$

$$k = \cos \chi. \tag{14}$$

Second, we compute the mean energy E_0 and energy flux F_E of precipitating electrons that are accelerated by a par-

allel potential drop $\Delta\Phi_\parallel$ in regions of upward field-aligned currents [*Knight*, 1972; *Lyons et al.*, 1979]:

$$F_E = F_1 \Delta\Phi_\parallel |j_\parallel|, \tag{15}$$

$$E_0 = e\Delta\Phi_\parallel, \tag{16}$$

$$\Delta\Phi_\parallel = \frac{e^2 n_e}{\sqrt{2\pi m_e kT_e}} \max(0, -j_\parallel). \tag{17}$$

Third, diffuse electron precipitation is modeled by assuming complete pitch angle scattering of electrons at 3.5 R_E [*Kennel and Petschek*, 1966]:

$$F_E = F_2 n_e (kT_e/2\pi m_e)^{\frac{1}{2}}, \tag{18}$$

$$E_0 = kT_e, \tag{19}$$

in which n_e, T_e, and m_e are the electron density, temperature, and mass, respectively, taken at the 3.5 R_E shell. Because the MHD formalism does not provide an electron temperature, we have included the empirical factors F_1 and F_2 to allow for an adjustment of the electron fluxes. In section 4.5 we show how a variation of these factors affects the substorm development.

The conductances are computed from the electron precipitation parameters using the empirical relation [*Robinson et al.*, 1987]:

$$\Sigma_P = [40E_0/(16 + E_0^2)]F_E^{1/2}, \tag{20}$$

$$\Sigma_H = 0.45E_0^{5/8}\Sigma_P. \tag{21}$$

Because the processes responsible for generating the conductance are given by the ionization rates which are in equilibrium with recombination, the Hall and Pedersen conductances from the different sources are added by taking their geometric mean.

Using the mapped FACs and ionospheric conductances, the potential equation is solved using a pseudospectral Galerkin method [*Canuto et al.*, 1987], and the ionospheric potential is mapped to the 3.5 R_E shell, where it is used as a boundary condition for the magnetospheric flow by taking $\mathbf{v} = (-\nabla\Phi) \times \mathbf{B}/B^2$.

2.3. Ground Magnetometer Calculation

The model provides all currents that are necessary to compute ground magnetic perturbations, except the ring current. In principle, Biot-Savart's law can be used to integrate over all currents in the magnetosphere and the ionosphere to determine the ground perturbation at a given location. However, this is a very costly procedure because the integration has to be done over a large volume and for many points in time. Because we are mostly interested in perturbations in the auroral zone, the calculations can be simplified by using Fukushima's theorem [*Fukushima*, 1976], which allows us to reduce the three-dimensional Biot-Savart integration to a two-dimensional integration over the ionospheric toroidal (equivalent) current. Thus we split the total ionospheric current, given by,

$$\mathbf{j} = -\Sigma \cdot \nabla\Phi, \tag{22}$$

into the poloidal and toroidal parts:

$$\mathbf{j} = \mathbf{j}_P + \mathbf{j}_T, \tag{23}$$

which satisfy

$$\nabla \cdot \mathbf{j}_T = 0, \tag{24}$$
$$\nabla \times \mathbf{j}_P = 0. \tag{25}$$

Thus the poloidal current $\mathbf{j}_P$ can be written in terms of a scalar potential Ψ:

$$\mathbf{j}_P = -\nabla \Psi, \tag{26}$$

which leads to a Laplace equation for Ψ:

$$\nabla^2 \Psi = -\nabla \cdot \mathbf{j}_P = -\nabla \cdot \mathbf{j}. \tag{27}$$

After solving for Ψ the toroidal current can be obtained from

$$\mathbf{j}_T = \mathbf{j} - \mathbf{j}_P = \mathbf{j} + \nabla \Psi. \tag{28}$$

As pointed out by *Fukushima* [1969,1976] and *Kamide et al.* [1981], the current system represented by $j_\parallel$ and $\mathbf{j}_P$ together produces no ground magnetic signature under the assumption of radial geomagnetic field lines. The latter assumption is certainly no worse than our assumption that all ionospheric currents flow in a spherical shell at a given altitude. Because the ground perturbations of $j_\parallel$ and $\mathbf{j}_P$ cancel, the perturbations are given by $\mathbf{j}_T$ and the magnetospheric currents. However, the latter currents will produce only a minor contribution at high latitudes compared to $\mathbf{j}_T$. Thus we obtain the ground magnetic perturbation by using Biot-Savart's law with $\mathbf{j}_T$:

$$\delta \mathbf{B}_{GR}(\mathbf{R}) = \frac{\mu_0}{4\pi} \int_{IO} \mathbf{j}_T(\mathbf{r}') \times \frac{\mathbf{R} - \mathbf{r}'}{|\mathbf{R} - \mathbf{r}'|^3} d\mathbf{r}', \tag{29}$$

where the integration extends over the spherical shell at 110 km that represents the ionosphere. $\mathbf{R}$ is the location, and $\delta \mathbf{B}_{GR}(\mathbf{R})$ is the perturbation at a ground magnetometer. In reality, the ground perturbation is expected to be modified by ground-induced currents. However, these depend on the conductivity of the Earth's outer layers, which are very difficult to quantify. We assume that this effect is small at the frequencies considered here, and we make no correction for these currents.

2.4. Initial Conditions

The initial conditions for the magnetic field are constructed from the superposition of the Earth's dipole over an equally strong mirror dipole, such that B_x vanishes at $x = 16\ R_E$. Sunward of the plane of symmetry at 16 R_E the field is replaced by the initial solar wind field. This procedure ensures a divergence-free transition from the constant solar wind field to the magnetospheric field. The dipole orientation in the simulation corresponds to the Earth's dipole orientation at 2230 UT on November 24, 1996 (the observed substorm onset), and is held constant during the entire run. The simulation box is initially filled with tenuous (0.1 cm^{-3}) and cold (5000 K) plasma of zero velocity. The simulation run is started with a southward interplanetary magnetic field
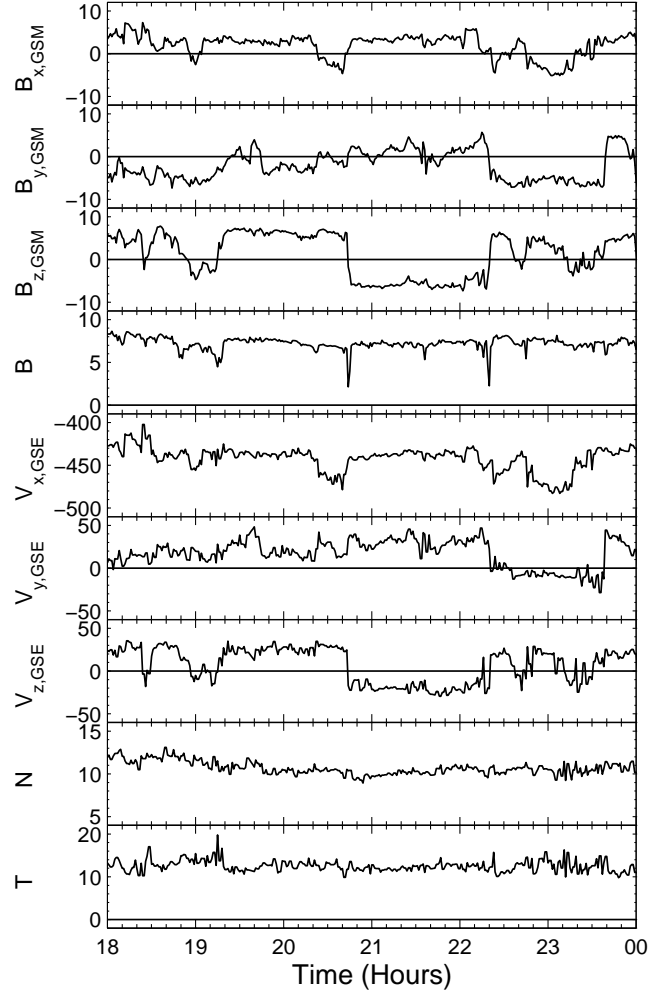
Figure 1. Wind interplanetary magnetic field (IMF) and solar wind data from (73,-18,8) R_E GSE on November 24, 1996. From top to bottom: the magnetic field components B_x, B_y, and B_z; the total magnetic field (all in nT, GSE); the flow velocity components V_x, V_y, and V_z (in km s^{-1}, GSE); the number density (in cm^{-3}); and the temperature (in eV).

(IMF) and average solar wind parameters in order to let the unphysical initial conditions evolve into a magnetospheric configuration. After 1 hour, we start to rotate the IMF vector toward its orientation at the beginning of the interval of interest (1800 UT). Thus 3 more hours (approximately three transit times) elapse until the beginning of the substorm growth phase. This ensures that the simulation of the substorm is not affected by the initial conditions.

3. Solar Wind Input

Wind observations of the solar wind and IMF are shown in Figure 1 for the period of 1800-2400 UT on November 24, 1996. Wind is during this time located at (73,-18,8) R_E in GSE coordinates. The data in Figure 1 are not time-shifted.

The solar wind velocity is almost constant throughout the entire interval. The solar wind number density is somewhat higher than normal (10-12 cm^{-3}) but fairly constant. There are also no major variations in the solar wind temperature. The IMF is predominantly northward until ∼2100 UT. At that time a major rotation of the IMF occurs, and the IMF becomes predominantly southward, until ∼2213 UT. After that time the IMF is predominantly northward again.

In order to use the Wind data as input for the simulation we propagate the Wind data ballistically at the prevailing solar wind speed (-420 km s^{-1}) to the inflow boundary of the simulation which is located 19 R_E upstream from Earth. We also compute the normal direction of the solar wind discontinuities using the minimum variance method [*Sonnerup and Cahill*, 1967, 1968] over the entire interval from 1800 to 2400 UT, which we find to be (0.88,-0.46,0.12) in GSE coordinates. This assumes that the solar wind roughly consists of layers that are all inclined by the same angle to the Sun-Earth line. We find that the magnetic field component in the normal direction is approximately constant, which justifies this assumption. On the basis of this normal direction we then propagate the solar wind and IMF into the simulation box. Hence we not only obtain a more accurate boundary condition, but we can also propagate the IMF B_x component into the simulation. The alternative, which entails setting the entire inflow boundary to the measured data, implies that the solar wind parameters are independent of Y and Z. In that situation, B_x cannot change, because that would violate Maxwell's equation $\nabla \cdot \mathbf{B} = 0$.

4. Results

4.1. Auroral Ground Magnetic Signature

Substorms are primarily identified by their ground magnetic signature. Figure 2 shows the comparison of ground magnetometers from the International Monitor for Auroral Geomagnetic Effects (IMAGE) chain across Scandinavia [*Viljanen and Häkkinen*, 1997] with the computed magnetograms from the model. The stations are ordered from north to south in Figure 2. Only the north-south component is shown here, because it has the largest and most distinct variations. Table 1 shows the magnetic latitude and the magnetic local time at 2230 UT of these stations. Beginning at ∼2100 UT the IMAGE magnetometers see the growth phase of the substorm, which is reflected in a small increase of the westward electrojet, i.e., a small negative perturbation. The computed magnetograms also show a negative perturbation; however, it is of much larger amplitude. At ∼2227 UT, IMAGE records the onset of a substorm expansion phase, marked by the rapid negative excursion at most of the stations. The computed magnetograms also show the expansion phase onset signature, marked by the accelerating decrease of the magnetic field values at most of the stations. However, the onset in the model occurs ∼5 min earlier. The modeled signature is also different from the observed one in other respects. First, there is a gradual decrease of the perturbation values long before the onset at some of the stations, whereas the IMAGE stations show no signs of an increasing electrojet before the commencement of onset, except for the small growth phase signature. Second, the expansion onset

Table 1. IMAGE[a] Magnetometer Stations

Station	Mag. latitude	MLT
LYR[b]	74.31	0243
HOR[c]	73.47	0222
BJN[d]	71.02	0202
AND[e]	67.13	0134
SOR[f]	67.16	0176
TRO[g]	66.94	0152
KIL[h]	66.06	0157
MAS[i]	65.97	0175
KEV[j]	65.69	0194
KIR[k]	65.07	0146
MUO[l]	64.72	0164
SOD[m]	63.61	0175
PEL[n]	63.46	0162
LOZ[o]	62.84	0222
OUJ[p]	60.91	0162
HOP[q]	60.33	0128
NUR[s]	57.62	0128

[a] International Monitor for Auroral Geomagnetic Effects,
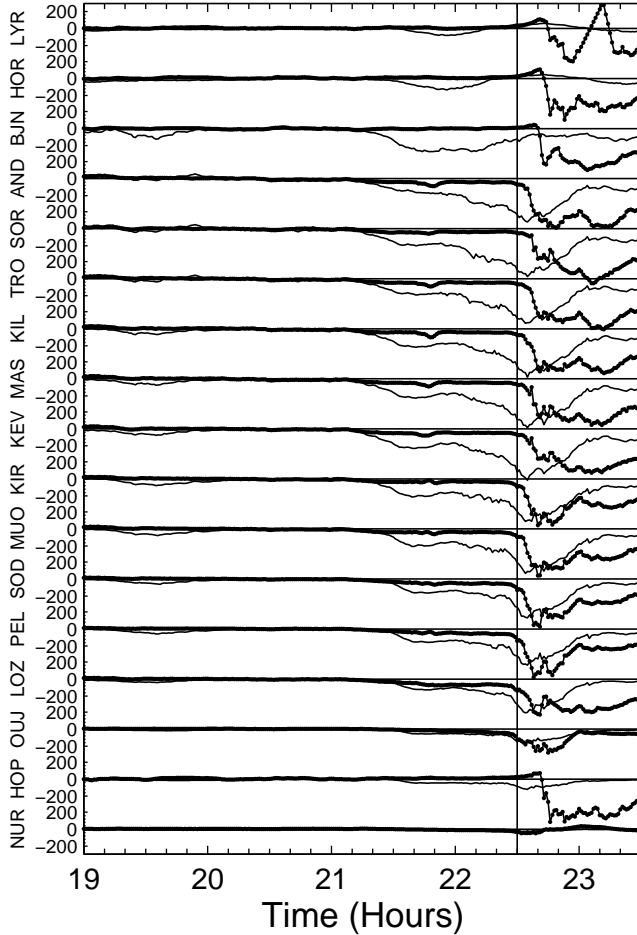[b]Longyearbyen, [c]Hornsund, [d]Bear Island, [e]Andenes, [f]Sørøya,
[g]Tromsø, [h]Kilpisjärvi, [i]Masi, [j]Kevo, [k]Kiruna, [l]Muonio,
[m]Sodankylä, [n]Pello, [o]Lovozero, [p]Oulujärvi, [q]Hopen Island,
[s]Nurmijärvi

Figure 2. Ground magnetometer traces from the International Monitor for Auroral Geomagnetic Effects (IMAGE) magnetometer chain on November 24, 1996 (thick dotted lines), and the comparison with the model result (thin solid line). Shown is the north-south (X) component in units of nT. The stations Longyearbyen (LYR), Hornsund (HOR), Bear Island (BJN), Andenes (AND), Sørøya (SOR), Tromsø (TRO), Kilpisjärvi (KIL), Masi (MAS), Kevo (KEV), Kiruna (KIR), Muonio (MUO), Sodankylä (SOD), Pello (PEL), Lovozero (LOZ), Oulujärvi (OUJ), Hopen Island (HOP), Nurmijärvi (NUR) are ordered in latitude from north to south, and their locations are given in Table 1.

proceeds slower in the model. Most IMAGE stations see a drop of several hundred nanoteslas within 5 min of onset, whereas the modeled perturbations show a rate that is slower by a factor of 1.5-3. Third, the expansion phase is much shorter in the simulation as compared to that in the data. The recovery at the IMAGE stations begins ∼30 min after the onset and lasts for more than 1 hour. At 2330 UT most IMAGE stations have not yet recovered to their presubstorm values. On the other hand, the model shows recovery beginning ∼15 min after onset. The recovery in the model is also more gradual and shorter, so that after 40 min most stations have recovered to nearly their presubstorm values.

The first onset signature in the IMAGE stations occurs at KIR (Kiruna), MUO (Muonio), SOD (Sodankylä), and PEL (Pello), i.e., between 63° and 65° magnetic latitude. The westward electrojet then expands both northward and southward in time. At the southward end the electrojet is bounded by the station NUR (Nurmijärvi) at which no expansion is observed, i.e., below 58° magnetic latitude. The IMAGE chain provides no bound at the northward end; thus the expansion proceeds beyond 74° magnetic latitude. The model result agrees very well with the observed southward expansion, with the exception of the HOP (Hopen Island) station. However, the OUJ (Oulujärvi) station, which is closely located to HOP, also sees only a very small expansion signature. Thus the model predicts the southward expansion to better than 2°, which is comparable to the model resolution. At the northward end of the electrojet the model does less well. At the stations BJN (Bear Island), HOR (Hornsund), and LYR (Longyearbyen), which all lie northward of 70° magnetic latitude, the model predicts no expansion but just a driven signature during the growth phase. Because the substorm expands to at least 74° magnetic latitude, the model prediction is off by at least 4° .

4.2. Polar Cap Parameters

Figure 3 shows time series of the magnetic field B_y and B_z components just upstream of the magnetopause near the subsolar point (Figures 3a and 3b), an ideal AL index from the model (i.e., the minimum of the north-south perturbation over the entire northern polar ionosphere)(Figure 3c), the polar cap magnetic flux from the model and from Polar VIS data (Figure 3d), the rate of change of the polar cap flux from the model (Figure 3e), the modeled cross polar cap potential in the northern hemisphere (Figure 3f), and the magnetic field elevation angle at GOES 8 (Figure 3g).

The magnetic field B_y and B_z components at the magnetopause clearly mark the arrival times of the IMF rotations at the magnetosphere; that is, the southward turning of B_z occurs at 2102 UT, and the northward turning occurs at 2236 UT. We do not claim that these are the actual arrival times in the magnetosphere, because we do not know the exact propagation characteristics of these discontinuities in the solar wind. However, these times are important for timing other signatures in the simulation. A few minutes after the arrival of the southward B_z at the magnetopause, the substorm growth phase begins with the expansion of the polar cap, a jump in the cross polar cap potential from ∼60 kV to ∼160 kV, and the growth of a driven electrojet, i.e., the gradual negative excursion of AL. The polar cap flux
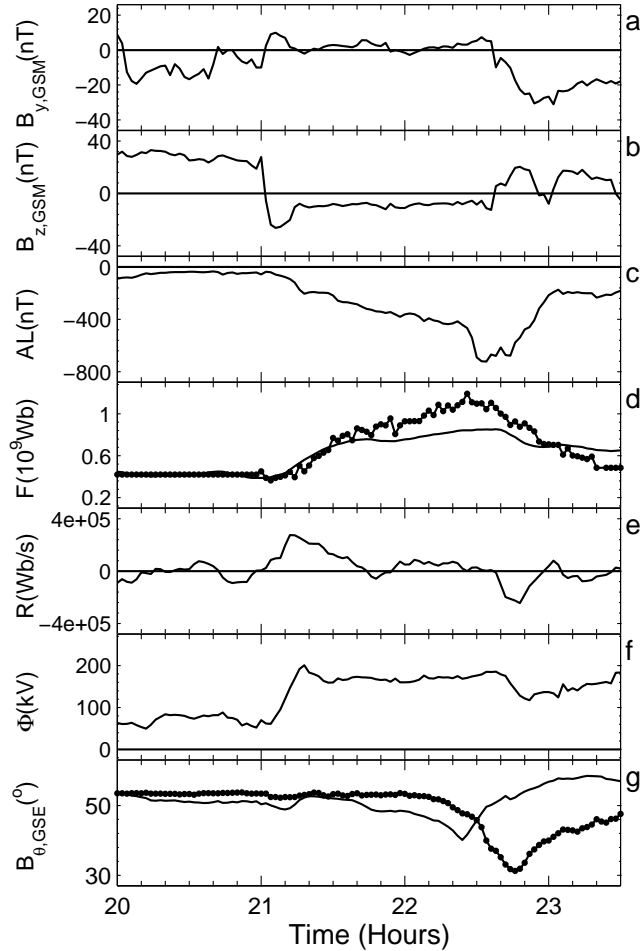
Figure 3. (a,b) Time series of the magnetic field B_y and B_z components in the magnetosheath at the subsolar magnetopause, (c) the modeled *AL* index, (d) the polar cap magnetic flux from the model (solid line) and from Polar Visible Imaging System (VIS) estimates (dotted line), (e) the rate of change of the polar cap flux as estimated from the model, (f) the cross polar cap potential from the model, and (g) the magnetic field elevation angle at GOES 8 from the model (solid line) and from GOES 8 (dotted line).

does not grow steady but grows initially faster (at a rate of $\sim 2 \times 10^5$ Wb s^{-1}), and then the growth slows down to a rate of $\sim 5 \times 10^4$ Wb s^{-1}. Comparison of the polar cap magnetic flux with data obtained from the VIS imager onboard the Polar satellite shows qualitatively the same behavior in the data. During the first 30 min the growth rate of the polar cap is roughly the same in the data and in the model. Later, until a maximum is reached, VIS shows a larger growth rate, and thus a higher maximum (1.15×10^9 Wb, versus 0.88×10^9 Wb for the model, i.e., a 23% difference). This difference is consistent with differences found in the lobe field strength (see below). However, the VIS data and the model have in common that the expansion of the polar cap continues until after the expansion phase onset. Note that the onset recorded by VIS occurs later than that in the model, i.e., at 2227 UT.

The *AL* index shows that the substorm expansion phase onset commencing at 2222 UT, before the northward turning of the magnetic field at the magnetopause. However, the only signature in the polar cap flux is, at most, a slight decrease in its growth rate. It takes ~ 10 more min after the *AL* onset until the polar cap area begins to shrink. The cross polar cap potential behaves similarly. At the *AL* onset there is a small increase of the potential, which reaches a maximum and then begins to decrease in sync with the polar cap flux. Both the decrease of the polar cap flux and the potential occur ~ 5 min after the northward IMF reaches the magnetopause.

In Plate 1 we present the ionosphere potential, field-aligned current (FAC), and the polar cap area, and we compare them to AMIE [*Richmond*, 1992; *Lu et al.*, 1995] results where appropriate. Plates 1a-1e show, respectively, the potential pattern from the model (MHD-POT), the AMIE potential pattern (AMIE-POT), the model FAC (MHD-FAC), the AMIE FAC distribution (AMIE-FAC), and the polar cap at four different times (from left to right: 2100, 2200, 2245, and 2300 UT). In Plate 1, downward FACs are positive.

At 2100 UT the southward IMF has not yet reached the magnetopause; thus the northward IMF with substantial B_x and B_y components leads to a two-cell potential pattern with a nearly circular positive cell over the pole and a kidney-shaped negative cell at lower latitudes in the dusk sector. At 2200 UT, well into the growth phase, the convection pattern is characterized by a typical two-cell convection pattern with strong day-night convection over the pole. This convection pattern persists with little modification into the expansion phase, as shown by the 2245 UT plots. Later, in the recovery phase, the northward IMF B_z and the strong negative IMF B_y produce a convection pattern with a positive cell over the pole and a negative cell at lower latitudes. This pattern is similar to the presubstorm pattern; however, the convection, is stronger and the negative cell is shifted towards the nightside.

The convection patterns produced by the model are generally very similar to those produced by AMIE. The main difference is the strength of the convection. The model predicts a cross polar cap potential that is about twice of that predicted by AMIE. We have found similar differences in a previous study [*Raeder et al.*, 1998], but we could not find a particular reason for the discrepancy. Here we also compare the field-aligned currents from our model with those from AMIE (Plates 1c and 1d). Both AMIE and the model
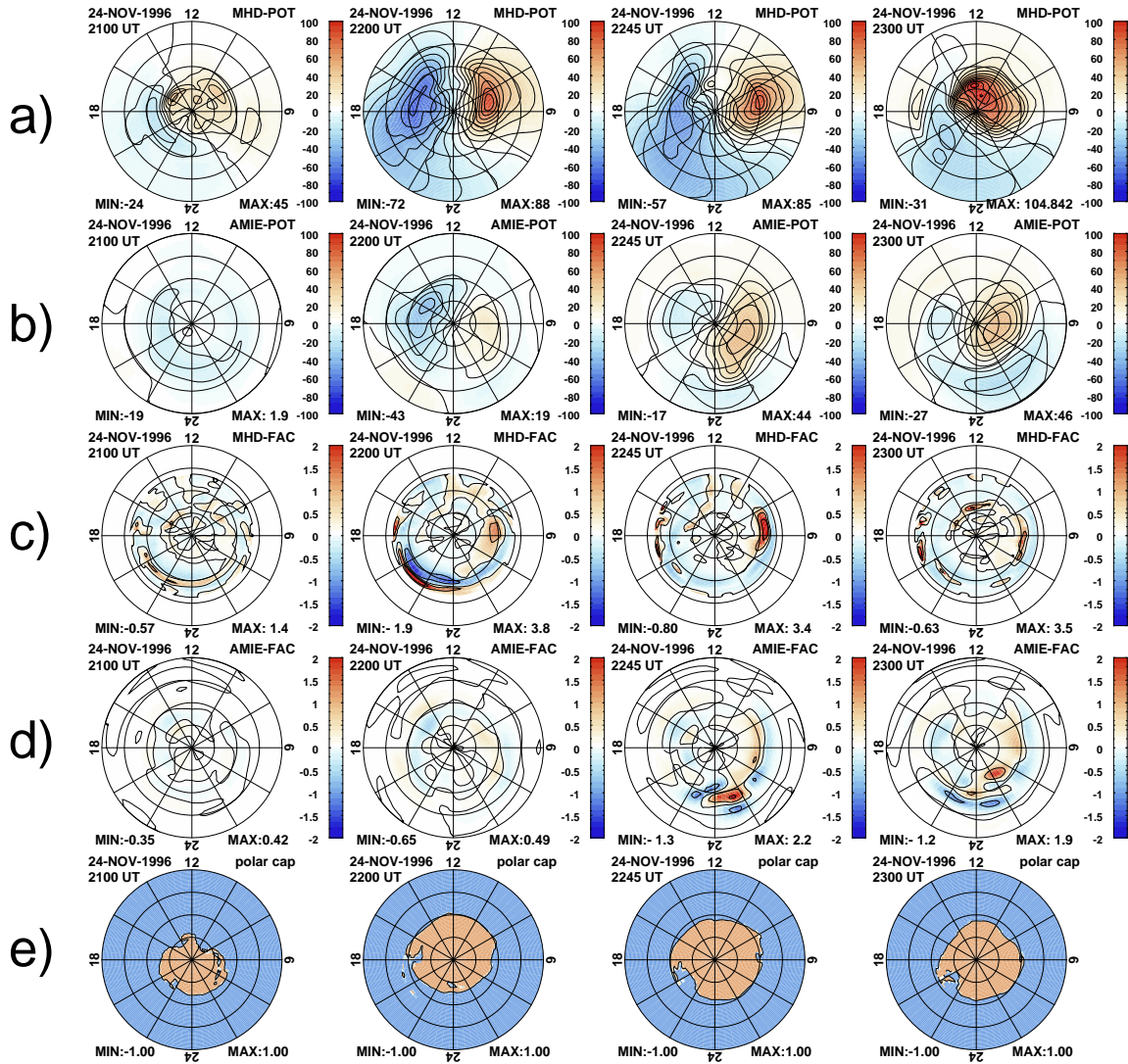
Plate 1. Ionospheric maps: (a) the potential pattern from the model (MHD-POT), (b) the assimilated mapping of ionospheric electrodynamics (AMIE) potential pattern (AMIE-POT), (c) the model FAC (MHD-FAC), (d) the AMIE FAC distribution (AMIE-FAC), and (e) the polar cap at four different times (from left to right: 2100, 2200, 2245, and 2300 UT). Potential contours are drawn at 10-kV intervals, and FAC contours are drawn at 0.5 μA m^{-2} intervals.

produce a fairly similar current pattern; in particular, the region 1 and cusp current distribution are comparable. At 2100 and 2200 UT the current produced by the model is significantly stronger than the current produced by AMIE, and the MHD model also predicts strong localized currents that are absent in the AMIE model. At these times it is quite plausible that the large potential in our model is caused, for example, by reconnection rates in the magnetosphere that are too high and drive FACs that are too strong. However, at later times (2245 and 2300 UT) the FACs produced by AMIE and those from the model are quite comparable. In particular, the magnitudes are very similar, and both models show strong localized currents, although in different locations. Thus, at these times it appears to be more likely that differences in the ionospheric conductances cause the discrepancy in the potential values. We have compared the conductance patterns of the two models (not shown here) and found that the differences are very complex and do not offer a simple explanation. Therefore, as we speculated in our previous study [*Raeder et al.*, 1998], it is unlikely that there is a single factor that causes the potential differences.

There is also a notable difference between AMIE and our model in the substorm current wedge signature. Our model predicts nightside region 1 current signatures that are reminiscent of a substorm current wedge already in the late growth phase at 2200 UT, i.e., the strong upward FAC in the 1900-2400 MLT sector and the downward current around 0600 MLT. These currents are essentially absent in the AMIE FAC pattern, and they produce the strong ground magnetic signature before onset in the modeled magnetograms (see Figure 2). Later, in the expansion phase, AMIE predicts a current wedge signature in the 2400-0200 MLT sector, whereas the model predicts the current wedge that essentially only consists of a downward current near 0600 MLT. Obviously, these current signatures are all generated in the tail, and we will discuss them in more detail with the tail signatures.

4.3. Signatures in the Near-Earth Tail

A typical near-Earth signature of substorm expansion onset is the dipolarization of the magnetic field. During the growth phase the field attains a stretched configuration, which at onset and during the expansion phase snaps back to a more dipolar geometry [*McPherron et al.*, 1973a, b; *Kokubun and McPherron*, 1981; *Nagai*, 1982; *Singer et al.*, 1985]. During this event, only the GOES 8 satellite was in a reasonable position to observe the field dipolarization, although it was far from local midnight, at $\sim$1730 MLT in the dusk magnetosphere. Figure 3g shows the comparison of the magnetic field elevation angle measured by GOES 8 with the model result. During the growth phase, stretching of the field occurs at GOES 8 as well as at the GOES 8 location in the model. Dipolarization commences at GOES 8 at $\sim$2245 UT, i.e., $\sim$18 min after the onset. In the model, dipolarization occurs earlier, at $\sim$2225 UT. Although the ionospheric onset occurs earlier in the model as well, the time delay between ionospheric onset and dipolarization at GOES 8 is much shorter in the model. In the model the dipolarization essentially coincides with the onset, while GOES 8 observes the dipolarization approximately 18 min after onset. This discrepancy indicates that there is a considerable difference in the formation and the evolution of the current wedge between the model and the data. This has already become evident from the current wedge location in the ionosphere, where the model places the current wedge signatures further to the flanks than the AMIE model does. Unlike the time difference, the magnitude of the dipolarization in the model compares well with the data.

In order to investigate the dipolarization further we show in Plate 2 cuts through the simulation domain in a plane parallel to the equatorial plane at Z=-3.3 R_E . Plate 2 shows, from left to right, $B_{z,\text{GSE}}$, $V_{x,\text{GSE}}$, and the temperature, at four different times (2200, 2215, 2245, and 2300 UT in Plates 2a-2d, respectively). The contour lines show B_z=0 and V_x=0, respectively. Note that because of the winter dipole orientation and the hinging of the tail, these cuts are not exactly in the plasma sheet everywhere; however, we have chosen the location of the cut such that it covers as much of the plasma sheet as possible.

At 2200 and 2215 UT (in the late growth phase) the tail is stretched, that is, the B_z is relatively weak in the near-Earth tail, and flows are predominantly earthward. At these times, there is already some indication of the beginning of a breakup in the tail in the morning sector where flows have become weakly tailward and B_z is reduced or slightly negative. The near-Earth plasma is at this time relatively cool with a maximum temperature of 12 keV.

At 2245 UT breakup has occurred with the formation of a new x line at around -17 R_E from Earth in the dawn sector and at $\sim$25 R_E from Earth in the dusk sector. Although one could argue that there is a single x line because of the continuous B_z=0 contour, there appear to be two distinct reconnection regions, each of which is associated with a channel of earthward flow. Of these two active regions, which only extend a few R_E in the Y direction, the one in the morningside is stronger and produces earthward flows of up to 300 km s^{-1}. Associated with these earthward flows is a substantial increase of B_z, i.e., the dipolarization of the field. This dipolarization is initially localized between 2300 and 0400 MLT, but spreads later both radially and around the flanks. Also associated with the dipolarization is a substantial heating of the near-Earth plasma. During the expansion phase (2245 UT) the near-Earth plasma temperature reaches $\sim$30 keV and then gradually cools during the recovery phase (2300 UT). This is the MHD equivalent of ring current injection. However, because MHD does not treat the drift motion of this plasma, it will not be trapped and form a ring current, but eventually escape through the dayside and flank boundaries.

At 2300 UT the recovery phase has begun. The x line is now generally retreating, but like the formation of the near-Earth neutral line, this process is not uniform across the tail. While the x line has moved beyond X=-25 R_E in the dawn sector, it is still closer to Earth in the dusk sector. However, there are no strong flows in either sector; thus, if reconnection is still occurring, it must be weak.

Although B_z and V_x are rather closely related in the tail, there is no one to one relationship between these quantities. In particular, B_z and V_x generally do not change sign in the same location. One reason is the dipole tilt which imposes an additional B_z component on the tail which is not uniform.
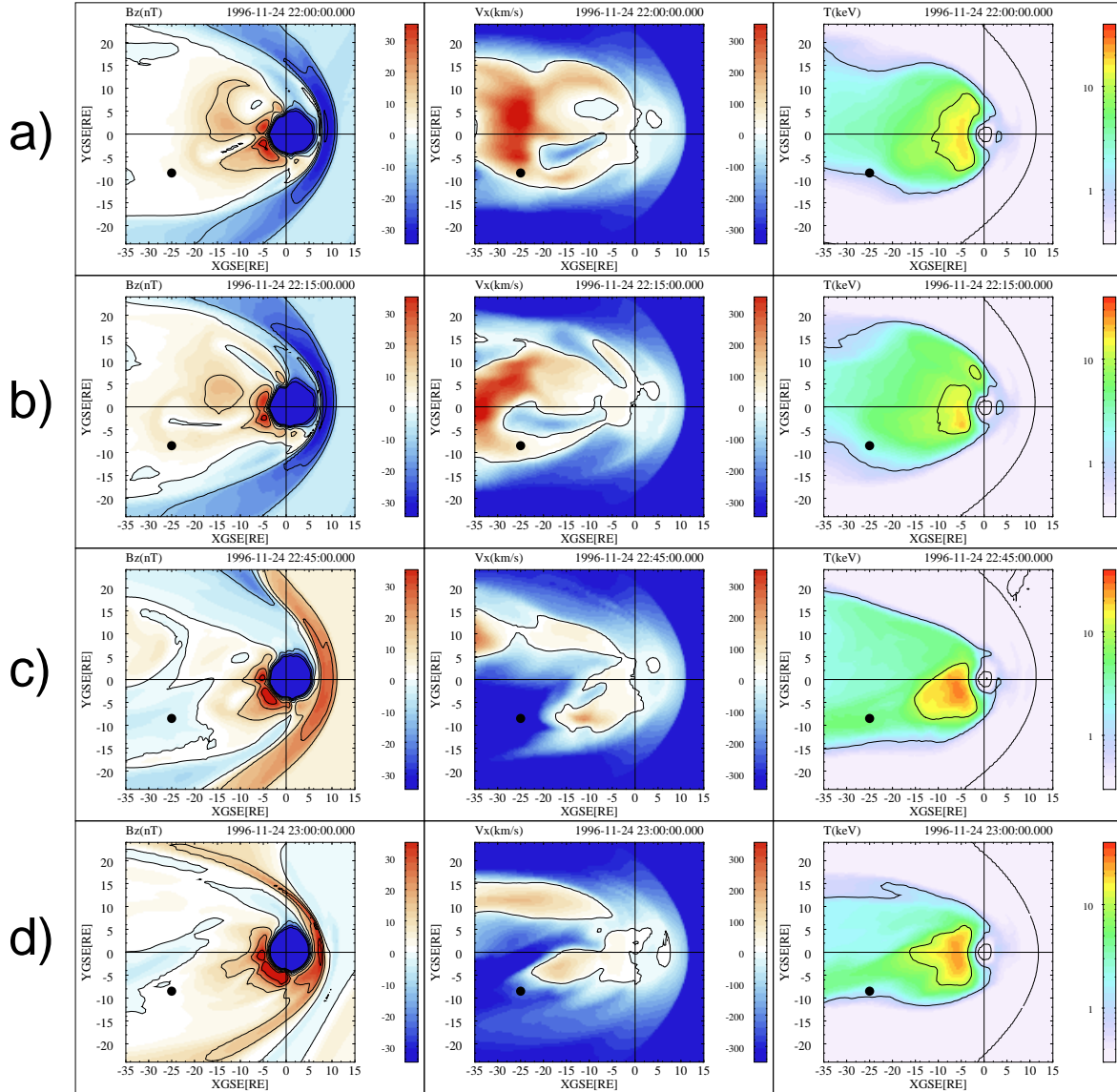
Plate 2. The magnetic field B_z component, the velocity V_x component, and the plasma temperature in a plane at Z_{GSE}=-3.3 R_E, at four different times: (a) 2200 UT, (b) 2215 UT, (c) 2245 UT, and (d) 2300 UT. Contours are drawn at the zero level for V_x, at 12 nT intervals for B_z, and at 1 and 10 keV for the temperature, respectively. The black dot marks Geotail's position.

Another reason is that some of the flows are almost parallel to the field, in particular, where $|B_z|$ is small. In that situation there is essentially no dynamic coupling between the flow and the field, because parallel flows are not associated with an electric field. Also, the entire x line can move with the large-scale flow, so that in the inertial frame the velocity **V** is shifted, while in the plasma rest frame the flows are still outward from the x line.

Also, a distinction between topological x lines and magnetic reconnection must be made. An x line is simply a geometry where the magnetic field is split into four topological distinct regions by two seperatrix surfaces whose intersection forms the x line but without necessarily having noticeable dynamic consequences. Reconnection, on the other hand, is not only characterized by an x line topology but also by significant energy conversion, i.e., fast (several hundred km s^{-1}) flows. Most likely there is a smooth transition between passive, topological x lines and magnetic reconnection. From Plate 1 it is evident that both occur in the tail.

It is also evident from Plate 1 that reconnection is highly localized in space and time. In particular, the reconnection geometry looks very unlike the cartoons that are usually drawn to envision this process [*Russell and McPherron*, 1973; *Hones*, 1977, 1979]. Because of the complex history of the tail imposed by the solar wind, the plasma and field parameters are nonuniform in space. Therefore it is not surprising that reconnection is strongly localized, because the reconnection process must depend critically on the local parameters.

Because of the rather "unorderly" character of the tail dynamics in the model, it is extremely difficult, if not impossible, to relate the dynamics of the tail to other substorm characteristics, for example, the electrojet, and to establish a clear time sequence of events. Although this simulation shows clearly reconnection before the auroral expansion phase onset, it is not clear if this is really the trigger of the expansion phase onset, i.e., if there is a clear relationship between that reconnection process and the subsequent enhancement of the electrojet.

4.4. Signatures in the Middle Tail

During this event, two satellites made observations in the middle tail around 30 R_E from Earth. IMP 8 was located at (-36,-3,10) R_E in GSE coordinates, i.e., in the northern lobe, while Geotail observed at times the plasma sheet and neutral sheet at (-25,-8,-3) R_E in GSE coordinates.

Figure 4 shows magnetic field data from IMP 8 and the comparison with the model. No plasma data were available from IMP 8. Because IMP 8 was located in the tail lobe, it clearly observes the loading of the tail with magnetic flux during the substorm growth phase [*Caan et al.*, 1975]. This signature commences at IMP 8 at 2138 UT with the gradual increase of B_x and the total field, accompanied by a small decrease of B_z. Thus the flaring angle and the magnetic flux in the tail increase. This increase ends abruptly at 2235 UT, when this process reverses, but at a faster rate. This behavior of the tail is usually explained as the loading of the tail with magnetic flux that is peeled off the dayside magnetosphere by reconnection and swept into the tail lobes, and by the subsequent removal of this flux by reconnection at the
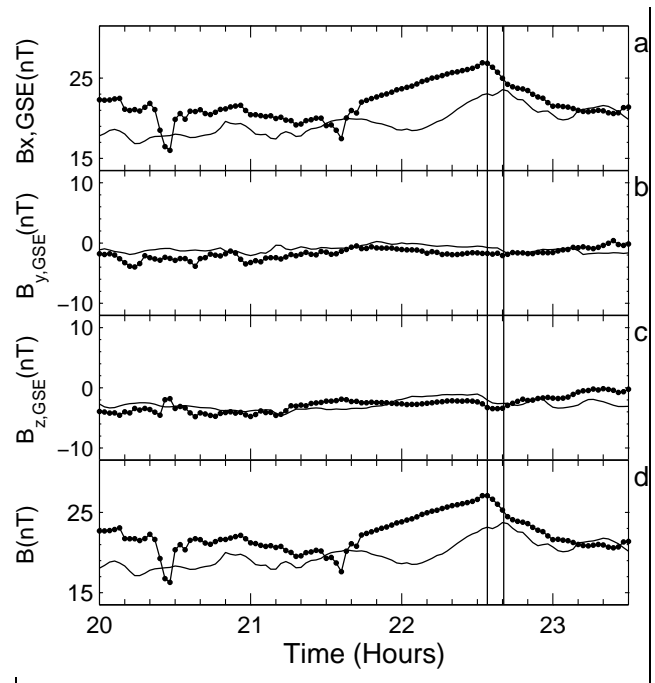
Figure 4. IMP 8 magnetic field data (dotted lines) and model results (solid lines) on November 24, 1996. GSE coordinates: (a) B_x, (b) B_y, (c) B_z, and (d) the total field. The two vertical lines mark the onset of the tail field reduction in the data and in the model, respectively.

near-Earth neutral line. The simulation shows qualitatively the same features but with noticeable differences. First, the increase of the tail flux does not begin with the arrival of the southward IMF at the magnetopause (see Figure 3) but starts ∼30 min later. This is possibly caused by increased tail reconnection during the initial growth phase and will be discussed in section 5. The second difference is the delayed unloading of the tail, which occurs ∼17 min after the onset. The unloading at IMP 8 is also delayed by 7 minutes with respect to the onset; thus the effective difference is ∼10 min. This difference is consistent with the difference that we found comparing the observed and the modeled time development of the polar cap area.

Figure 5 shows magnetic field and plasma data from Geotail and the comparison with the model results. Figure 5 shows, from top to bottom, the magnetic field B_x, B_y, and B_z components [*Kokubun et al.*, 1994]; the plasma flow V_x component; the plasma number density; the plasma pressure; and the plasma temperature. Plasma data from the Comprehensive Plasma Instrumentation (CPI) instrument [*Frank et al.*, 1994] and the Low Energy Particles (LEP) instrument [*Mukai et al.*, 1994] (lines with open circles) are shown. The heavy solid line shows the result from the model at the Geotail location. There are substantial differences between the model and the data. Considering the dynamic nature of the tail plasma sheet and the fact that large gradients in all plasma and field parameters exist in the tail, this is not surprising. To illustrate what difference a small perturbation of the spacecraft location makes, we have also produced time series at locations that are 2 R_E above and below the Geotail location. The upper and lower bounds of the shaded areas in Figure 5 are defined by these time series. The shaded areas essentially bracket the observations. Thus, in order to predict the Geotail observations, a model would not only have to produce the plasma and field values correctly but also their location better than within 2 R_E. Of course, this is extremely difficult, considering that the tail is in constant motion owing to the buffeting from the solar wind and IMF and owing to its internal dynamics.

Despite this difficulty, there are important features that can be compared and conclusions that can be drawn. From the magnetic field B_x component it is clear that Geotail traverses the plasma sheet several times during this event. The model predicts only one excursion at the nominal Geotail position, but for the position 2 R_E below Geotail it would predict only southern lobe observations, and for the position 2 R_E above Geotail it would essentially predict a northern lobe position. Thus the plasma sheet in the model is at most 4 R_E thick between 2100 and 2330 UT, and it is most likely much thinner in reality. Since the model resolution in the Z direction is ∼0.3 R_E, the plasma sheet is just barely resolved.

The Geotail B_y signature is rather uneventful; however, the model predicts a large B_y signature just at the substorm onset. This signature is most likely caused by the formation of a flux rope. The B_y spike is also very localized because it does not appear in the time series taken 2 R_E below Geotail.

The magnetic field B_z component is positive during the entire growth phase, while the flow is generally earthward. At about the expansion phase onset the flow turns tailward, and shortly thereafter B_z becomes negative. This indicates
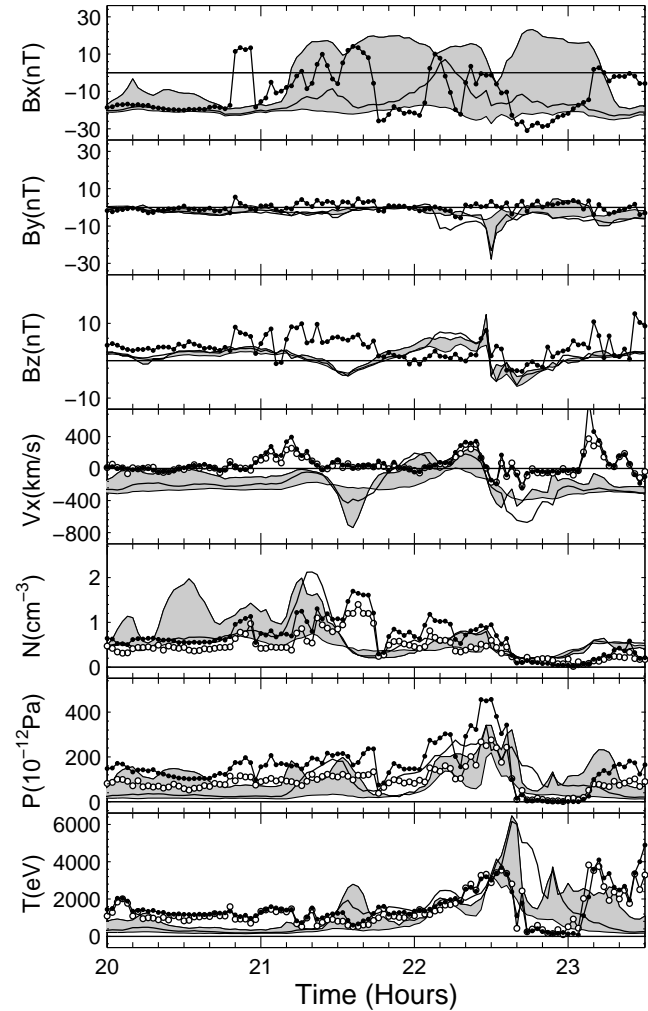
Figure 5. Geotail magnetic field and plasma data and comparison with the model results, on November 24, 1996. The dotted lines are magnetic field and plasma data from the Magnetic Field Experiment (MGF) and Low Energy Particle (LEP) experiment, respectively. Data represented with open circles are from the Comprehensive Plasma Instrumentation (CPI) instrument. Model results at the nominal Geotail position are drawn with a heavy solid line. The shaded area is bounded by time series taken from the model at locations that are 2 R_E above and below Geotail, respectively.

that a new x line has formed earthward of Geotail. The behavior of the simulation is generally similar, except that the flow is tailward for most of the growth phase, and for a brief interval around 2135 UT where B_z becomes negative and the flow becomes strongly tailward. However, a characteristic feature in both the Geotail data and the simulation is the 15-min surge before the B_z turns southward, during which B_z becomes stronger northward (to ~5 nT) and the flow becomes strongly earthward (to ~300 km s^{-1}). This surge is also present to some extent in the plasma density and very prominently in the plasma pressure and temperature. *Petrukovich et al.* [1999] have found such pressure surges in their survey of substorms (including this one) and attribute them to two reconnection regions, one earthward and one tailward of Geotail. Our simulation confirms this view. As the second and third panels of Plate 2 show, Geotail is located just tailward of the dawnside near-Earth neutral line. A second neutral line (not visible in Plate 2) is located further tailward. Thus plasma is piling up between these two neutral lines, causing the pressure peak observed by Geotail.

4.5. Parameter Variations

As outlined in section 2, our model depends on several parameters that arise from the parameterization of kinetic processes. These are, in particular, the anomalous resistivity and the energy flux of electrons into the ionosphere. The latter determines the auroral conductances in the nightside and thus affects magnetospheric convection. We have varied these parameters, i.e., the resistivity threshold δ and scale factor α (equation (9)), and the energy flux factors F_1 and F_2 (equations (15) and (18)) over a wide range of values. We found that for most parameter combinations no substorm occurs. Thus the results presented above (which will be referred to as Run 1 in the remainder of this paper) are for a certain parameter combination that produces an onset at about the correct time and with roughly the correct magnitude, as measured by the ground magnetometer perturbations. Specifically, the parameters for this run were δ=0.65, α=0.05, and F_1=F_2=4.

Figure 6 shows ground magnetic perturbations from three runs with parameter combinations that do not produce a substorm. Specifically, in Run 2 we have set the precipitation parameters F_1 and F_2 to a value of 1.5, i.e., about a factor 2.6 lower than that in Run 1, but we have kept the anomalous resistivity parameters the same as those in Run 1. In Run 3 we have set the anomalous resistivity to zero (α=0), and in Run 4 we have lowered the threshold for the anomalous resistivity (δ=0.4) and increased its scale (α=0.2), while keeping the ionosphere parameters the same as those in Run 1.

None of these runs produces a substorm. Instead, the magnetosphere enters a driven mode in which the electrojet slowly increases during the growth phase and then slowly decreases after the IMF turns northward. Also, for these runs there is no significant loading and unloading in the tail (via comparison with the IMP 8 magnetic field, not shown here). Thus, instead of loading the tail during the growth phase with magnetic flux and energy and then unloading it during the expansion phase, the tail enters a state of steady convection in which dayside reconnection is apparently well balanced by reconnection in the tail. Although
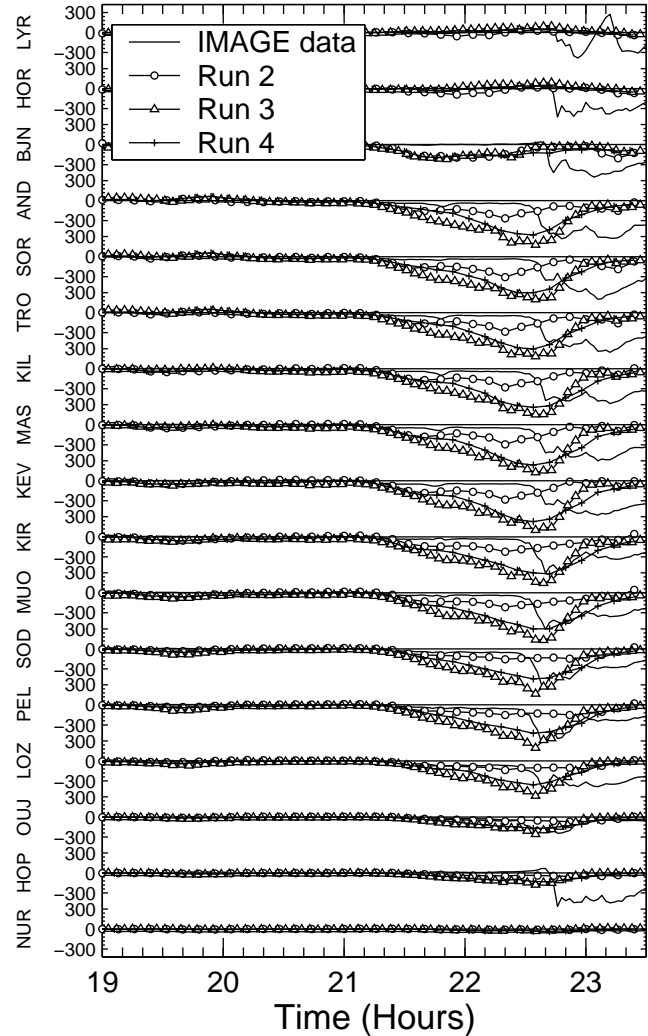
Figure 6. Comparison of IMAGE ground magnetometer recordings on November 24, 1996, with the results from three different simulation runs that did not produce a substorm (see text for details). The format of Figure 6 is the same as that in Figure 2.

this is clearly a wrong solution for this event, it is not completely unphysical, and such steady magnetospheric convection (SMC, sometimes called "convection bays") events have indeed been observed [*Yahnin et al.*, 1994].

5. Summary and Discussion

The GEM substorm challenge event provides us with the unique opportunity to compare our model with data and to assess its validity with respect to substorm dynamics. We find that the model generally compares well with the observations, in particular, that the model reproduces the prominent substorm features that could be expected from a fluid model. Of course, other substorm features, like Pi2 bursts or particle injections, are beyond the scope of the model.

The substorm dynamics produced by the model follows essentially the phenomenological near-Earth neutral line (NENL) model [*McPherron et al.*, 1973b; *McPherron*, 1991; *Baker et al.*, 1996, 1999]. During the growth phase, magnetic flux is removed from the dayside magnetosphere via reconnection and swept into the tail. This creates an imbalance between dayside and nightside reconnection which leads to an increase in tail magnetic flux, which for this event is observed by the Polar VIS instrument (expanding polar cap) and by IMP 8 in the tail lobe. Near expansion phase onset, one or more new neutral lines form in the tail relatively close to Earth, and eventually they begin reconnecting lobe flux. As a result, tail reconnection becomes stronger than dayside reconnection, and the tail flux begins to decrease. However, neither the data nor the simulation can tell us in detail at this point how reconnection connects to the auroral features. The data analysis is hampered by the sparsity of observation points, and the simulation is limited by too coarse resolution and the fact that the plasma sheet is very dynamic and that reconnection is localized and occurs in several regions. Also, because the IMF turned northward at or shortly after the onset, it is difficult to say by how much the nightside reconnection rate is increasing. However, the model is in very good agreement with the data in predicting that a new neutral line forms earthward of Geotail (>-25 R_E) in close association with expansion phase onset. This and the fact that the model also produces other common substorm signatures (ground perturbations, dipolarization, and current wedge) give us confidence that the model is essentially based on the correct physics and that the results are meaningful.

However, the differences between the model and the data give us an important lesson as to the shortcomings of the model and where improvements are needed. A number of these differences indicate that the reconnection rates in the model are too high. First, the polar cap potential is consistently higher than the potential estimated by AMIE. Although the AMIE potential depends on assumptions, for example, the ionospheric conductance, it appears to be unlikely that the resulting errors in the potential would be as high as a factor 2-3. Second, the model exhibits a strong, driven electrojet during the growth phase that is at least a factor of 5 stronger than the observed ground signature. This is also evident from the FAC distribution, which shows a current wedge like distribution already during the growth phase. Obviously, these currents are generated in the tail by reconnection. At the Geotail location the model predicts tailward flow during much of the growth phase, whereas Geotail observes either no flow or earthward flows. Only in the late growth phase does the model reproduce the tail flows well. Thus the presubstorm x line in the model lies too close to Earth, at least in the Geotail meridian. Third, as a consequence of the excessive convection, the model stores less magnetic flux and energy in the lobes as the data indicate. This then leads to the short recovery phase in the model.

It is difficult to point to a single cause for these differences, and quite possibly there are more causes than one:

1. As we have shown the electron precipitation, and thus the ionospheric conductance, substantially influences magnetospheric convection and thus the substorm dynamics. Unfortunately, no direct measurement of conductance is possible, and thus we cannot calibrate our conductance model very well. Statistical models are not of much use here, because they average over the instantaneous features and also because they are in part based on the same empirical relations [*Robinson et al.*, 1987] that we use in the model. On the other hand, there is much room for improving our model. For example, a dynamic, self-consistent ionosphere-thermosphere model like the Coupled Thermosphere Ionosphere Model (CTIM) [*Fuller-Rowell et al.*, 1996] could be used in place of the empirical Robinson formulae to compute the conductances from the electron precipitation parameters using first principles. Also, one could use a model like the Rice Convection Model (RCM) [*Wolf*, 1983; *Toffoletto et al.*, 1996] to compute the drift of inner magnetosphere electrons and thus improve the calculation of diffuse electron precipitation. It is also possible to use space-based EUV images of the aurora to infer electron precipitation characteristics [*Lummerzheim et al.*, 1997; *Germany et al.*, 1997], which could then be used to correct the model conductances by data assimilation methods.

2. The model of anomalous resistivity used in the simulation is based on the assumption that some current-dependent kinetic process causes sufficient turbulence to scatter electrons to the effect of substantial anomalous diffusion. Although there is experimental evidence that such processes indeed occur in the tail [*Sigsbee et al.*, this issue; see also *Cattell and Mozer*, 1986; *Cattell*, 1996; *Cattell et al.*, 1998], no constraints are available, and in particular, no details are known about the dependence on plasma parameters. Recent studies of the reconnection process using various modeling approaches [*Birn and Hesse*, 2000; *Hesse et al.*, 2000; *Otto*, 2000] also indicate that processes that are not included in MHD, for example, the Hall term or the $\nabla \cdot P_e$ term, where P_e is the electron pressure tensor, have a substantial influence on reconnection rates. Thus there is considerable room to improve the anomalous resistivity model, for example, by parameterizing results from kinetic models. Furthermore, numerical resistivity is present in our model (like any other model) and difficult to quantify. Because the simulation of this substorm required anomalous resistivity to a certain degree, whereas running the model without anomalous resistivity (i.e., reconnection is solely caused by numerical resistivity) produced no substorm, it is quite likely that numerical resistivity plays only a minor role. However, its effects cannot be ruled out entirely.

3. Our model does not contain a ring current. This is because of the MHD formalism which does not allow for

gradient and curvature drifts. Thus plasma cannot be captured in the inner magnetosphere, but instead $\mathbf{E} \times \mathbf{B}$ drifts out. In other words, there is never a closed drift shell for any plasma energy. As a consequence, the plasma pressure peaks in the tail at around 6 R_E at pressure values that are far lower than typical plasma pressure values of the ring current [*Lui et al.*, 1987]. Thus the presence of a ring current would inflate the inner magnetosphere and possibly push the x line farther tailward. A ring current would also produce more realistic region 2 currents in the ionosphere, which should partly shield the inner magnetosphere from convection and thus also modify the substorm behavior of the tail. We note that our model produces one ingredient of the ring current formation, namely, plasma injection. From Plate 2 it is evident that during the expansion phase plasma is transported earthward and energized to ∼2-3 times the presubstorm temperature. Thus coupling with a ring current model like the RCM may improve our model considerably.

A key result of this study is the dependence of the substorm dynamics on the parameterization of inherently kinetic processes, i.e., auroral electron acceleration and anomalous resistivity in the magnetosphere. This is on one hand troublesome, because an ab initio model should not depend on parameters. On the other hand, it gives us some insight into the physics of substorms. First, the magnetospheric steady convection mode that occurs for many parameter combinations is indeed observed at times [*Yahnin et al.*, 1994]. However, it is not known what conditions lead to a SMC mode as opposed to a substorm. The solar wind and IMF parameters are essentially the same, thus the reason for the difference must be internal to the magnetosphere or ionosphere. Our results indicate that the reasons may be found either in the ionospheric control of magnetospheric convection or in the details of the reconnection process in the tail. Second, the parameter dependence points to some incompleteness of the NENL model. The NENL model makes no reference to the ionospheric response; instead, it treats the ionosphere as a passive recipient of energy from the magnetosphere. As our results show, there must be some significant feedback from the ionosphere to the tail, which controls in a yet undetermined way the expansion phase onset. This is not to say that the ionosphere is solely responsible like in some models [*Kan*, 1993]. Rather, a number of ingredients have to come together, in particular, tail loading, near-Earth reconnection, and an ionosphere that permits fast reconnection and dipolarization in the tail and thus an explosive energy release into the ionosphere.

References

Baker, D. N., T. I. Pulkkinen, V. Angelopoulos, W. Baumjohann, and R. L. McPherron, Neutral line model of substorms: Past results and present view, *J. Geophys. Res.*, *101*, 12,975, 1996.

Baker, D. N., T. I. Pulkkinen, J. Büchner, and A. J. Klimas, Substorms: A global instability of the magnetosphere-ionosphere system, *J. Geophys. Res.*, *104*, 14,601, 1999.

Birn, J., and M. Hesse, Geospace Environment Modeling (GEM) magnetic reconnection challenge: Resistive tearing, anisotropic pressure and Hall effects, *J. Geophys. Res.*, in press, 2000.

Caan, M. N., R. L. McPherron, and C. T. Russell, Substorm and interplanetary magnetic field effects on the geomagnetic tail lobes, *J. Geophys. Res.*, *80*, 191, 1975.

Canuto, C., M. Y. Hussaini, A. Quarteroni, and T. A. Zang, *Spectral Methods in Fluid Dynamics*, Springer-Verlag, New York, 1987.

Cattell, C. A., Experimental evaluation of the Lundquist number for the Earth's magnetopause and magnetotail, *J. Geophys. Res.*, *101*, 27,309, 1996.

Cattell, C. A., and F. S. Mozer, Experimental determination of the dominant wave mode in the active near-Earth magnetotail, *Geophys. Res. Lett.*, *13*, 221, 1986.

Cattell, C., J. Wygant, J. Dombeck, F. S. Mozer, M. Temerin, and C. T. Russell, Observations of large amplitude parallel electric field wave packets at the plasma sheet boundary, *Geophys. Res. Lett.*, *25*, 857, 1998.

Evans, C. R., and J. F. Hawley, Simulation of magnetohydrodynamic flows: A constrained transport method, *Astrophys. J.*, *332*, 659, 1988.

Fedder, J. A., and J. G. Lyon, The solar wind–magnetosphere–ionosphere current–voltage relationship, *Geophys. Res. Lett.*, *14*, 880, 1987.

Fedder, J. A., S. P. Slinker, J. G. Lyon, and R. D. Elphinstone, Global numerical simulation of the growth phase and the expansion onset for a substorm observed by Viking, *J. Geophys. Res.*, *100*, 19,083, 1995.

Fox, G. C., M. A. Johnson, G. A. Lyzenga, S. W. Otto, J. K. Salmon, and D. W. Walker, *Solving Problems on Concurrent Processors*, Prentice-Hall, Englewood Cliffs, N.J., 1988.

Frank, L. A., K. L. Ackerson, W. R. Paterson, J. A. Lee, M. R. English, and G. L. Pickett, The Comprehensive Plasma Instrumentation (CPI) for the Geotail spacecraft, *J. Geomagn. Geoelectr.*, *46*, 23, 1994.

Fukushima, N., Equivalence in ground magnetic effect of Chapman-Vestine's and Birkeland-Alfven's current systems for polar magnetic storms, *Rep. Ionos. Space Res. Jpn.*, *22*, 219, 1969.

Fukushima, N., Generalized theorem for no ground magnetic effect of vertical currents connected with Pedersen currents in the uniform conducting ionosphere, *Rep. Ionos. Space Res. Jpn.*, *30*, 35, 1976.

Fuller-Rowell, T. J., D. Rees, S. Quegan, R. J. Moffett, M. V. Codrescu, and G. H. Millward, A coupled thermosphere-ionosphere model (CTIM), in *STEP Report*, edited by R. W. Schunk, p. 217, Sci. Comm. on Sol. Terr. Phys., Boulder, Colo., 1996.

Germany, G. A., G. K. Parks, M. Brittnacher, J. Cumnock, D. Lummerzheim, J. F. Spann, L. Chen, P. G. Richards, and F. J. Rich,

Remote determination of auroral energy characteristics during substorm activity, *Geophys. Res. Lett.*, *24*, 995, 1997.

Gombosi, T. I., D. L. DeZeeuw, C. P. T. Groth, K. G. Powell, and P. Song, The length of the magnetotail for northward IMF: Results of 3D MHD simulations, in *Physics of Space Plasmas (1998)*, edited by T. Chang and J. R. Jasperse, vol. 15, p. 121, Mass. Inst. of Technol. Center for Theoretical Geo/Cosmo Plasma Physics, Cambridge, Mass., 1998.

Goodrich, C. C., J. G. Lyon, M. Wiltberger, R. E. Lopez, and K. Papadopoulos, An overview of the impact of the January 10-11, 1997 magnetic cloud on the magnetosphere via global MHD simulation, *Geophys. Res. Lett.*, *25*, 2537, 1998.

Harten, A., and G. Zwas, Self-adjusting hybrid schemes for shock computations, *J. Comput. Phys.*, *9*, 568, 1972.

Hesse, M., J. Birn, and M. Kuznetsova, Collisionless magnetic reconnection: Electron processes and transport modeling, *J. Geophys. Res.*, in press, 2000.

Hirsch, C., *Numerical Computation of Internal and External Flow*, vol. 2, John Wiley, New York, 1990.

Hones, E. W., Substorm processes in the magnetotail: Comments on: "On hot tenuous plasmas, fireballs, and boundary layers in the Earth's magnetotail" by L. A. Frank, K. L. Ackerson, and R. P. Lepping, *J. Geophys. Res.*, *82*, 5633, 1977.

Hones, E. W., Transient phenomena in the magnetotail and their relation to substorms, *Space Sci. Rev.*, *23*, 393, 1979.

Hoshino, M., Forced magnetic reconnection in a plasma sheet with localized resistivity profile excited by lower hybrid drift type instability, *J. Geophys. Res.*, *96*, 11,555, 1991.

Janhunen, P., T. I. Pulkkinen, and K. Kauristie, Auroral fading in ionosphere-magnetosphere coupling model: Implications for possible mechanisms, *Geophys. Res. Lett.*, *22*, 2049, 1995.

Kamide, Y., and S. Matsushita, Simulation studies of ionospheric electric fields and currents in relation to field aligned currents, 1, Quiet periods, *J. Geophys. Res.*, *84*, 4083, 1979.

Kamide, Y., A. D. Richmond, and S. Matsushita, Estimation of ionospheric electric fields, ionospheric currents, and field-aligned currents from ground magnetic records, *J. Geophys. Res.*, *86*, 801, 1981.

Kan, J. R., A global magnetosphere - ionosphere coupling model of substorms, *J. Geophys. Res.*, *98*, 17,263, 1993.

Kennel, C. F., and H. E. Petschek, Limit on stably trapped particle fluxes, *J. Geophys. Res.*, *71*, 1, 1966.

Knight, S., Parallel electric fields, *Planet. Space Sci.*, *21*, 741, 1972.

Kokubun, S., and R. L. McPherron, Substorm signatures at synchronous altitude, *J. Geophys. Res.*, *86*, 11,265, 1981.

Kokubun, S., T. Yamamoto, M. H. Acuna, K. Hayashi, K. Shiokawa, and H. Kawano, The Geotail magnetic field experiment, *J. Geomagn. Geoelectr.*, *46*, 7, 1994.

Lu, G., et al., Characteristics of ionospheric convection and field-aligned current in the dayside cusp region convection pattern, *J. Geophys. Res.*, *100*, 11,845, 1995.

Lui, A. T. Y., R. W. McEntire, and S. M. Krimigis, Evolution of the ring current during two geomagnetic storms, *J. Geophys. Res.*, *92*, 7459, 1987.

Lummerzheim, D., M. Brittnacher, D. Evans, G. A. Germany, G. K. Parks, M. H. Rees, and J. F. Spann, High time resolution study of the hemispheric power carried by energetic electrons into the ionosphere during the May 19/20, 1996 auroral activity, *Geophys. Res. Lett.*, *24*, 987, 1997.

Lyon, J. G., R. E. Lopez, C. C. Goodrich, M. Wiltberger, and K. Papadopoulos, Simulation of the March 9, 1995, substorm: Auroral brightening and the onset of lobe reconnection, *Geophys. Res. Lett.*, *25*, 3039, 1998.

Lyons, L. R., D. Evans, and R. Lundin, An observed relation between magnetic field aligned electric fields and downward electron energy fluxes in the vicinity of auroral forms, *J. Geophys. Res.*, *84*, 457, 1979.

Lyons, L. R., R. L. McPherron, E. Zesta, G. D. Reeves, J. B. Sigwarth, and L. A. Frank, Timing of substorm signatures during the November 24, 1996, Geospace Environment Modeling event, *J. Geophys. Res.*, this issue(a).

Lyons, L. R., J. M. Ruhoniemi, and G. Lu, Substorm-associated changes in large-scale convection during the November 24, 1996, Geospace Environment Modeling event, *J. Geophys. Res.*, this issue(b).

McPherron, R. L., Physical processes producing magnetospheric substorms and magnetic storms, in *Geomagnetism*, edited by J. Jacobs, vol. 4, p. 593, Academic, San Diego, Calif., 1991.

McPherron, R. L., G. K. Parks, D. S. Colburn, and M. Montgomery, Satellite studies of magnetospheric substorms on August 15, 1968, 2, Solar wind and inner magnetosphere, *J. Geophys. Res.*, *78*, 3054, 1973a.

McPherron, R. L., C. T. Russell, and M. P. Aubry, Satellite studies of magnetospheric substorms on August 15, 1968, 9, Phenomenological model for substorms, *J. Geophys. Res.*, *78*, 3131, 1973b.

Moen, J., and A. Brekke, The solar flux influence on quiet time conductances in the auroral ionosphere, *Geophys. Res. Lett.*, *20*, 971, 1993.

Mukai, T., S. Machida, Y. Saito, M. Hirahara, T. Terasawa, N. Kaya, T. Obara, M. Ejiri, and A. Nishida, The low energy particle (LEP) experiment onboard the Geotail satellite, *J. of Geomag. Geoelectr.*, *46*, 669, 1994.

Nagai, T., Observed magnetic substorm signatures at synchronous altitude, *J. Geophys. Res.*, *87*, 4405, 1982.

Ogino, T., A three-dimensional MHD simulation of the interaction of the solar wind with the Earth's magnetosphere: The generation of field-aligned currents, *J. Geophys. Res.*, *91*, 6791, 1986.

Otto, A., Geospace Environment Modeling (GEM) magnetic reconnection challenge: MHD and Hall MHD - constant and current dependent resistivity models, *J. Geophys. Res.*, in press, 2000.

Petrukovich, A. A., T. Mukai, S. Kokubun, S. A. Romanov, Y. Saito, T. Yamamoto, and L. M. Zelenyi, Substorm-associated pressure variations in the magnetotail plasma sheet, *J. Geophys. Res.*, *104*, 4501, 1999.

Pulkkinen, T. I., D. N. Baker, M. Wiltberger, C. Goodrich, R. E. Lopez, and J. G. Lyon, Pseudobreakup and substorm onset: Observations and MHD simulations compared, *J. Geophys. Res.*, *103*, 14,847, 1998.

Raeder, J., Global MHD simulations of the dynamics of the magnetosphere: Weak and strong solar wind forcing, in *Proceedings of the Second International Conference on Substorms*, edited by J. R. Kan, J. D. Craven, and S.-I. Akasofu, p. 561, Geophys. Inst., Univ. of Alaska, Fairbanks, 1995.

Raeder, J., Modeling the magnetosphere for northward interplanetary magnetic field: Effects of electrical resistivity, *J. Geophys. Res.*, *104*, 17,357, 1999.

Raeder, J., and R. L. McPherron, Global MHD simulations of the substorm current wedge and dipolarization, in *Substorms-4*, edited by S. Kokubun and Y. Kamide, p. 343, Kluwer Acad., Norwell, Mass., 1998.

Raeder, J., J. Berchem, and M. Ashour-Abdalla, The importance of small scale processes in global MHD simulations: Some numerical experiments, in *The Physics of Space Plasmas*, edited by

T. Chang and J. R. Jasperse, vol. 14, p. 403, Mass. Inst. of Technol. Center for Theoretical Geo/Cosmo Plasma Physics, Cambridge, Mass., 1996.

Raeder, J., J. Berchem, and M. Ashour-Abdalla, The Geospace Environment Modeling grand challenge: Results from a Global Geospace Circulation Model, *J. Geophys. Res.*, *103*, 14,787, 1998.

Richmond, A. D., Assimilative mapping of ionospheric electrodynamics, *Adv. Space Res.*, *6(1)*, 59, 1992.

Robinson, R. M., R. R. Vondrak, K. Miller, T. Dabbs, and D. Hardy, On calculating ionospheric conductances from the flux and energy of precipitating electrons, *J. Geophys. Res.*, *92*, 2565, 1987.

Russell, C. T., and R. L. McPherron, The magnetotail and substorms, *Space Sci. Rev.*, *15*, 205, 1973.

Sato, T., and T. Hayashi, Externally driven magnetic reconnection as a powerful magnetic energy converter, *Phys. Fluids*, *22*, 1189, 1979.

Sigsbee, K., C. A. Cattell, F. S. Mozer, K. Tsuruda, and S. Kokubun, Geotail observations of low-frequency waves from 0.001 to 16 Hz during the November 24, 1996, Geospace Environment Modeling substorm challenge event, *J. Geophys. Res.*, this issue.

Singer, H. J., W. J. Hughes, C. Gelpi, and B. G. Ledley, Magnetic disturbances in the vicinity of synchronous orbit and the substorm current wedge: A case study, *J. Geophys. Res.*, *90*, 9583, 1985.

Sonnerup, B. U. O., and L. J. Cahill, Magnetopause structure and attitude from Explorer 12 observations, *J. Geophys. Res.*, *72*, 171, 1967.

Sonnerup, B. U. O., and L. J. Cahill, Explorer 12 observations of the magnetopause current layer, *J. Geophys. Res.*, *73*, 1757, 1968.

Tanaka, T., Generation mechanisms for magnetosphere-ionosphere current systems deduced from a three-dimensional MHD simulation of the solar wind-magnetosphere-ionosphere coupling processes, *J. Geophys. Res.*, *100*, 12,057, 1995.

Toffoletto, F. R., R. W. Spiro, R. A. Wolf, M. Hesse, and J. Birn, Self-consistent modeling of inner magnetospheric convection, in *Third International Conference on Substorms (ICS-3)*, edited by E. J. Rolfe and B. Kaldeich, Eur. Space Agency Spec. Publ., ESA SP-389, 223, 1996.

Viljanen, A., and L. Häkkinen, IMAGE magnetometer network, Eur. Space Agency Spec. Publ., ESA SP-1198, 111, 1997.

Walker, R. J., T. Ogino, J. Raeder, and M. Ashour-Abdalla, A global magnetohydrodynamic simulation of the magnetosphere when the interplanetary magnetic field is southward: The onset of magnetotail reconnection, *J. Geophys. Res.*, *98*, 17,235, 1993.

Winglee, R. M., and J. D. Menietti, Auroral activity associated with pressure pulses and substorms: A comparison between global fluid modeling and Viking UV imaging, *J. Geophys. Res.*, *103*, 9189, 1998.

Wolf, R. A., The quasi-static (slow flow) region of the magnetosphere, in *Solar Terrestrial Physics*, edited by R. L. Carovillano and J. M. Forbes, p. 303, D. Reidel, Norwell, Mass., 1983.

Yahnin, A., et al., Features of steady magnetospheric convection, *J. Geophys. Res.*, *99*, 4039, 1994.

L. A. Frank, W. R. Paterson, and J. B. Sigwarth, Dep. of Physics and Astronomy, The University of Iowa, Iowa City, IA 52242.

S. Kokubun, Solar Terrestrial Laboratory, Nagoya University, Honohara 3-13, Toyokawa Aichi 442, Japan.

G. Lu, High Altitude Observatory, NCAR, Boulder, CO 80307.

R. L. McPherron and J. Raeder, Institute of Geophysics and Planetary Physics, University of California at Los Angeles, 405 Hilgard Avenue, Los Angeles, CA 90095-1567 (rmc@igpp.ucla.edu; jraeder@igpp.ucla.edu).

T. Mukai, Institute of Space and Astronautical Sciences, 3-1-1 Yoshinodai, Sagamihara, Kanagawa 229, Japan.

H. J. Singer, Space Environment Center, NOAA, Boulder, CO 80303.

J. A. Slavin, NASA Goddard Space Flight Center, Greenbelt, MD 20771.